AIAA JOURNAL
Vol. 36, No. 5, May 1998

Prediction of High-Lift Flows Using Turbulent Closure Models

Christopher L. Rumsey* and Thomas B. Gatski†
NASA Langley Research Center, Hampton, Virginia 23681-2199
Susan X. Ying‡
The Boeing Company, Long Beach, California 90807-4418
and
Arild Bertelrud§
Analytical Services and Materials, Inc., Hampton, Virginia 23681-2199

The flow over two different multielement airfoil configurations is computed using linear eddy-viscosity turbulence models and a nonlinear explicit algebraic stress model. Transition locations that were recently measured using hot film on one of the configurations are presented, and the effect of transition location on the computed solutions is explored. Deficiencies in wake profile computations are found to be attributable in large part to poor boundary-layer prediction on the generating element rather than on inadequate turbulence modeling in the wake. Using measured transition locations for the main element improves the prediction of the main-element boundary-layer thickness, skin friction, and wake profile shape. However, using measured transition locations on the slat still yields poor slat–wake predictions. The computation of the slat flowfield remains a major problem in the successful prediction of multielement flows. In general, the nonlinear, explicit algebraic stress turbulence model yields results that are similar to those of the linear eddy-viscosity models.

I. Introduction

A. Overview

THE prediction of high-lift (multielement airfoil) flowfields currently represents a difficult challenge for the computational fluid dynamics (CFD) and turbulence modeling community. Even in two dimensions, state-of-the-art CFD codes fail to predict trends with regard to Reynolds number or flap and slat rigging changes with sufficient accuracy.[1] Without the capability to consistently predict trends using CFD, aircraft designers must rely on heuristic techniques and wind-tunnel experiments, which can present additional difficulties when the results are scaled up to flight Reynolds numbers.[2–4]

The flow around a multielement airfoil or wing is inherently complex. Variations in angle of attack and different slat and flap settings often present very different and distinct challenges. For example, for typical landing configurations viscous effects can dominate compressibility effects near stall, whereas for typical takeoff configurations compressibility can dominate the stall physics.[5] Also, flap separation is often seen at low to moderate angles of attack, whereas at stall the aft portion of the main element is often unloaded and the flow over the flap surface is attached.[1]

Although high-lift devices work essentially because they manipulate the inviscid flow,[2] viscous effects are crucial and are coupled strongly to the inviscid effects. According to Meredith,[6] some of the viscous features that can affect two-dimensional multielement systems include boundary-layer transition, shock and boundary-layer interactions, viscous wake interactions, confluent wakes and boundary layers, and separated flow regions. Some important insights into the physical processes that govern high-lift aerodynamics were summarized by Smith in his landmark 1975 paper.[7] In particular, he described several effects that contribute to the improved high-lift characteristics of multiple elements.

A great volume of work on high-lift flows, both computational and experimental, has built up since 1975. (See, for example, discussions in the papers by Lynch et al.,[1] Haines,[2] Woodward and Lean,[8] Thibert et al.,[9] and Valarezo.[10]) Computational methods range from coupled viscous and inviscid methods, e.g., Ref. 11, through incompressible and compressible Reynolds-averaged Navier–Stokes approaches (see the review paper by Ying[5]). Several CFD code validation efforts have been undertaken. For example, an AGARD three-element takeoff configuration, tested in the early 1970s and subsequently used as part of a battery of AGARD test cases,[12] was recently used as a code validation challenge[13] by the Computational Fluid Dynamics Society of Canada. Experiments have also been performed in the NASA Langley Low Turbulence Pressure Tunnel (LTPT)[14,15] on McDonnell Douglas (MD) three-element landing configurations; some of those configurations were used as test cases in a CFD Challenge Workshop held at NASA Langley Research Center in 1993. Several papers have been written that describe various aspects of experimental testing on those configurations.[16–20]

Since the NASA CFD Challenge Workshop, many CFD results have been reported for the MD three-element configurations, obtained from a variety of numerical schemes for the Navier–Stokes equations. The incompressible Navier–Stokes code INS2D, which uses both point-matched and overset grids, has been used extensively to assess the capability of CFD to model trends that occur with configuration changes, to assess the tunnel-wall and grid density effects, and to evaluate the use of different turbulence models.[21–24] This code has also been coupled with a transition-prediction methodology.[25] Compressible Navier–Stokes codes have been used as well. Jones et al.[26] used the code CFL3D with overset grids to compute flow over the two-dimensional MD three-element configurations and three-dimensional flow over wings with flaps. The structured grid codes OVERFLOW and TLNS3D and the unstructured-grid codes NSU2D and FUN2D have also been applied to the two-dimensional MD configurations.[5,27,28]

B. Code Validation Issues

Overall, comparisons of CFD results with experimental results for the two-dimensional MD three-element configurations have been somewhat ambiguous. Considering the inherent complexity of the flowfield, CFD results are surprisingly good, particularly with regard

Received Aug. 26, 1997; revision received Jan. 12, 1998; accepted for publication Jan. 12, 1998.

*Research Scientist, Fluid Mechanics and Acoustics Division, Mail Stop 128. Senior Member AIAA.
†Senior Research Scientist, Fluid Mechanics and Acoustics Division, Mail Stop 128.
‡Principal Engineer, Flight Performance, Mail Code 078-0421. Senior Member AIAA.
§Senior Scientist, Mail Stop 170. Senior Member AIAA.

to surface pressures. Unfortunately, the predicted trends that occur with Reynolds number and configuration changes are not accurate enough to meet the needs of wing designers, and the maximum lift coefficient and the angle of attack at which maximum lift occurs tend to be overpredicted.[1] However, the reasons for these deficiencies are not clear at this time. Possible causes are inadequate modeling by the CFD codes, e.g., turbulence and transition models, and the likelihood that the CFD codes are not simulating the same configuration as in the experiment.

The first possibility may play a role because most of the turbulence models in use today are eddy-viscosity one- and two-equation models that do not account for effects such as curvature or anisotropy. Missing effects such as those may be important in certain regions of multielement flowfields. Additionally, most CFD codes prescribe rather than predict transition locations; those locations can have a significant effect on the solution.[29,30] Moreover, the transition process is usually not modeled. Instead, the eddy viscosity is generally switched on at transition points. More sophisticated transition models, such as that employed by Cebeci[31] (in an interactive boundary-layer code that is coupled with an algebraic turbulence model), are currently not widely used. The presence of laminar separation bubbles, which are usually associated with high peak suctions and steep adverse pressure gradients,[4] are also generally not taken into account.

The second possibility, that the CFD codes may not simulate the same configuration as in the experiment, arises particularly because of questions regarding the deviation from two-dimensionality in experimental tests and the applicability of two-dimensional CFD simulations to such flows. Additionally, the effects of surface roughness, tunnel turbulence, external tunnel devices, and structural model deformations must be considered. Because multielement airfoil flow appears to be highly sensitive to these parameters, the determination of precisely why a CFD simulation deviates from a given experimental result is often difficult. To cite an example of this experimental sensitivity, a three-element airfoil section that represents the Airbus 310 wing section at 59% span was found to yield a negative trend of $C_{L\max}$ with increasing Reynolds numbers between 6 and 16 $\times 10^6$ for an unpolished model but a positive trend when the model was polished.[32]

C. Turbulence Model Studies

Rogers et al.[24] showed that several different eddy-viscosity models are generally consistent in their prediction of the flow over the MD three-element configuration. The differences between the turbulence model predictions are generally smaller than the differences between computational and experimental results. Further perspective may be gained on the issue of turbulence modeling by considering both the experimental and computational results for different configurations. Squire[33] and Agoropoulos and Squire[34] compared computed velocity profiles and turbulence quantities with the experimental results from a study of flow over a two-element model; this study was designed to explore the interaction between the slat wake and the boundary layer of the main wing. They describe the merging process with three regimes: the unmerged region, when the wake and boundary layer are separated by a potential core; the initial merging region, when the outer part of the wake and the inner part of the boundary layer are unaffected; and the region of full merging, which results in a new, thicker boundary layer. By using the incompressible Navier–Stokes equations with a k–ε turbulence model and an algebraic stress model (ASM), Agoropoulos and Squire[34] found that both models agreed well with the experimental results in the initial stages of the merging, with somewhat better results using the ASM. Decelerated flows were predicted with the same accuracy as those in constant pressure.

In addition to computing the landing configurations for the CFD Challenge Workshop, Anderson and Bonhaus[35] computed the flow over an MD three-element takeoff configuration by using the unstructured code FUN2D. They compared those computations with the experimental results (including turbulent shear stress data) of Nakayama et al.[36] The one-equation eddy-viscosity turbulence model of Spalart and Allmaras[37] (S–A) was used; turbulent shear stress profiles were found to be in overall reasonable agreement with the experiment. Peak levels were underpredicted on the flap, but results in that region may not have been sufficiently grid converged.

Lien and Leschziner[38] and Lien et al.[39] computed the flow over both a separated single-element ONERA airfoil and a two-element (main element and flap) NLR-7301 airfoil.[40] They compared results that were obtained using k–ε two-equation eddy-viscosity models with those obtained using full second-moment Reynolds stress closure models on the ONERA airfoil and found the latter models to be generally superior. However, all of the turbulence models performed poorly in the far wake, in regions where the turbulence production over dissipation was low. The k–ε eddy-viscosity model performed fairly well on the NLR-7301 airfoil, although the wake mixing was incorrect and insufficient mixing was predicted between the wing wake and flap boundary layer. These inaccuracies were attributed to the inability of the k–ε the model to represent curvature–turbulence interaction.

Godin et al.[41] also computed flow over the NLR-7301 airfoil using the one- and two-equation eddy-viscosity turbulence models of Spalart and Allmaras[37] and Menter[42] [shear stress transport (SST)]. Good agreement was generally noted for both models, although the SST model was more accurate in separated flow regions and the S–A model performed better for attached flows and wakes, including the region in which the wake and boundary layer merge. Turbulent shear stress profiles generally agreed better with the experimental results than the k–ε eddy-viscosity model results of Lien et al.,[39] but velocity profiles were similar. Cao and Kusunose,[29] Jasper et al.,[43] and Fritz[44] also computed this two-dimensional flow using various zero-, one-, and two-equation eddy-viscosity models. Generally positive agreement with experimental data was obtained for lift, surface pressures, and velocity profiles, although the zero-equation (algebraic) model used by Jasper et al.[43] resulted in less accurate predictions of boundary-layer parameters and stall onset in comparison with the one-equation model. No comparisons with Reynolds stress data were made in these three references.

The results for the NLR-7301 airfoil support the findings of Rogers et al.[24] (for the MD configuration) that, although noticeable differences are certainly evident at a detailed level, many eddy-viscosity turbulence models tend overall to have only relatively minor effects on global properties for multielement airfoil predictions. (This conclusion is, of course, dependent on the particulars of the flowfield in question. For example, for flows with boundary-layer separation, models such as the S–A and SST models have been shown to be superior to the standard Jones–Launder version of the k–ε model.[42,45]) The question of whether more advanced nonlinear turbulence models would produce significantly better results for multielement airfoils remains open.

D. Focus of this Paper

Because of the complexity and interdependence of many factors in high-lift computing and experimentation, focusing solely on the subject of turbulence modeling without regard for other factors seems inappropriate. We, therefore, take a somewhat broader approach. The purpose of this paper is to facilitate a greater understanding of the issues that surround CFD validation against high-lift wind-tunnel tests. As a consequence, this work focuses on both experimental and numerical issues. Specifically, the purpose is threefold: to introduce a subset of transition locations for the two-dimensional MD three-element configuration that were recently measured in the LTPT with hot film, to demonstrate the effect of transition location on CFD solutions, and to explore the effects of a nonlinear explicit algebraic Reynolds stress turbulence model[46] on the Computational Fluid Dynamics solution for both the AGARD takeoff configuration[12,13] and the MD landing configuration.[16–20] By taking this approach, we hope not only to determine the impact of modeling the nonlinear Reynolds stress terms but also to demonstrate the importance (and difficulty) of accurately modeling the wind-tunnel experiment, particularly with regard to the transition process.

This paper is organized as follows. In Sec. II, two airfoil configurations are presented and some numerical sensitivity issues are discussed. Section III presents the experimental transition test, and Secs. IV and V describe the CFD computer code and turbulence models, respectively. Section VI presents results and discussion for the two configurations. Section VII gives conclusions.

II. Numerical Sensitivity, Airfoil Configurations, and CFD Grids

Two multielement configurations are investigated in this paper. Both employ one-to-one point connectivity across grid zones. Grids with one-to-one point connectivity ensure conservation across boundaries and provide improved continuity of grid spacing at zonal interfaces, although the grid generation for this type of grid is substantially more difficult than for overset or unstructured grids.

The grids employed in the current study were developed based on extensive grid sensitivity studies that were published previously for both CFL3D[26] and other codes[21–23,28] for similar configurations. Those studies indicate that velocity profiles are more sensitive to grid density than are surface pressures and lift coefficient. When between 100,000 and 200,000 grid points are used for point-matched grids that are similar to the grids used in the current study, further refinement yields only minor differences in the computed velocity profiles.[23] These earlier studies also indicate the importance of having sufficient resolution (via grid clustering) in all boundary layers, wakes, and their confluent regions. The grids used in the current study have over 100,000 grid points with minimum normal wall grid spacings that yield an average $y+$ of approximately 0.3–0.4 for their respective freestream Reynolds numbers. The grids are also clustered in the wake and confluent regions of each element.

The first case is a three-element configuration that is defined as case A2 in a battery of AGARD test cases[12] and was used as a test case for the code validation challenge[13] by the Computational Fluid Dynamics Society of Canada in June 1996. Although tested in a wind tunnel with solid walls, this AGARD test case is performed on a free-air grid with a far-field extent of approximately 10 chords. (The original model has a stowed chord of $c = 0.7635$ m, and the tunnel-height-to-chord ratio is $H/c = 5.19$.) The slat is positioned at an angle of 25 deg, and the single-slotted flap has a moderate deflection angle of 20 deg, which is typical of a takeoff configuration. The four-zone grid has 114,908 grid points. This configuration is computed at $M = 0.197$ and $Re = 3.52 \times 10^6$ based on the stowed-geometry chord. Transition is tripped on the main element at $x/c = 0.125$ on both the upper and lower surface and is free on the slat and flap.

The second configuration is a three-element MD configuration[16–20] that was tested in the LTPT and used as a test case in the CFD Challenge Workshop held at NASA Langley Research Center in 1993. The model has a stowed chord of $c = 0.5588$ m, and the tunnel-height-to-chord ratio is $H/c = 4.09$. The particular slat and flap settings employed include a slat deflection of 30 deg, a slat gap of 2.95%, a slat overhang of −2.5%, a flap deflection of 30 deg, a flap gap of 1.27%, and a flap overhang of 0.25%. This rigging designation is referred to as 30P-30N and is typical of a landing configuration. This configuration is computed using both a free-air grid with far-field extent of approximately $15c$, as well as a grid that models an angle of incidence of 19 deg with the LTPT walls. This latter grid extends $15c$ upstream and $19c$ downstream of the model to avoid the possibility of inflow and outflow boundary influence on the solution, although the actual LTPT test section does not extend this far. The grid without walls is a four-zone grid with 135,428 grid points, and the grid with walls is a five-zone grid with 138,389 grid points. Both are computed at $M = 0.2$ and $Re = 9 \times 10^6$ based on stowed-geometry chord. In the wind-tunnel test, transition is free on each of the elements. Figure 1 shows the grid topology for the MD 30P-30N configuration. The grid topology for the AGARD configuration is similar and can be found in Ref. 47.

III. Description of Transition Test and Data

A subset of transition data recently taken in the LTPT is presented here for the MD three-element configuration. The hot-film sensors are similar to those used by Nakayama et al.[48] for a similar configuration in the same wind tunnel. The sensors are thin nickel films on a 0.05-mm polyimide substrate. The sensors are arranged in a straight streamwise array at 73.4% span, whereas most pressure taps are located at 50% span. Side-wall suction is used to maintain approximate two-dimensionality of the flow. However, the suction is optimized for an angle of attack of 16 deg. Up through this angle of attack, the discrepancies in pressure distribution between the 50%-span row and an auxiliary-pressure-tap row near the hot films are generally moderate. Above 16 deg, three-dimensionality becomes more pronounced; hence, the three-dimensionality may be a contributing factor in results shown later. Details can be found in Ref. 49.

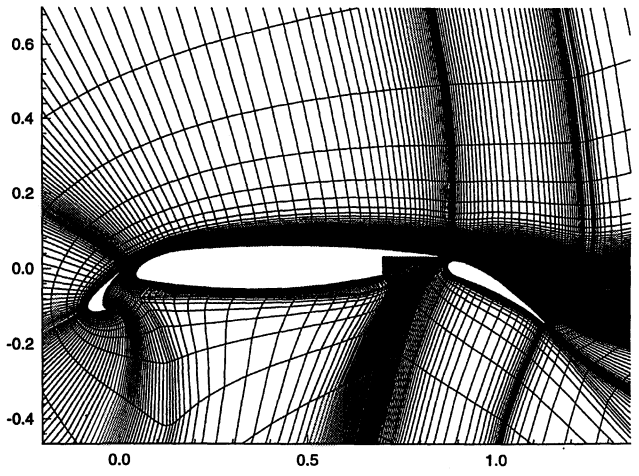

Fig. 1 30P-30N grid, with every other grid point removed.

Three-dimensionality affects the data in two ways. First, span-loading variations, which manifest themselves as variations in effective angle of attack, cause the locations of suction peaks and stagnation points to be displaced in the chordwise direction. Second, separated or low-shear regions, as well as brackets, for example, may cause spanwise flow that alters the transition data. Assuming that the experimental data are available, the upper surface chordwise effects may be accounted for in the CFD code at least in part by relating the transition to the distance downstream of the suction peak as opposed to using an absolute geometric location. However, for the MD cases in this paper, this step is not necessary because the computed suction-peak locations agree with those in the experiment to within a distance that is less than the densest pitch of the hot films. Spanwise effects are not easily taken into account.

Transition locations are determined based on information from 359 surface hot films on the three elements. The beginning and end of transition are extracted from an analysis of a combination of standard deviation, skewness, and flatness factors of the hot-film signals, plus in most cases an additional examination of the signal traces for auto- or cross correlations. Note that, even though the films are located at 2.54-mm pitch (or $\Delta s/c = 0.0045$) in the densest regions, the flows at higher angles of attack have fairly short transition regions, so that only one or two films pick up the feature.

Table 1 lists the starting and ending transition locations for the 30P-30N configuration at two angles of attack, along with locations of the suction peaks. Results are given in terms of both the surface coordinate s/c (where $s/c = 0$ corresponds to the location on the forward part of each element in the stowed position where $y/c = 0$) as well as the deployed x/c coordinate. Depending on the location, the data are accurate to between $\Delta s/c = \pm 0.002$ and 0.005. Possible film-sheet influence on transition has not been taken into account. An N/a for the transition start (S) or end (E) indicates that a definitive start or end to transition, respectively, was not detected before the cusp on the lower surfaces of the slat and main elements or before the trailing edge on the flap. The L for the upper suction peak at 19 deg indicates that the location is actually on the lower side of the element when the slat is in its rotated position.

Note the discrepancy that is present in the location of the flap suction peak between the 50%-span station (mid) and the auxiliary station near the hot films at 73.4% span (aux.) at both angles of attack. Computed suction peaks agree best with the mid data. This table represents only a subset of the transition-location measurements taken. More details on the experimental database can be found in Refs. 49 and 50.

IV. Description of Computer Code

The computer code CFL3D[51–54] solves the three-dimensional time-dependent Reynolds-averaged compressible Navier–Stokes

Table 1 Hot-film transition data for 30P-30N configuration with $M = 0.2$ and $Re = 9 \times 10^6$

	8 deg		19 deg	
Surface feature	s/c	x/c	s/c	x/c
Slat				
Lower suction peak	N/a	——	N/a	——
Lower transition S	N/a	——	N/a	——
Lower transition E	N/a	——	N/a	——
Upper suction peak	0.015	−0.084	0.006	−0.0852L
Upper transition S	0.030	−0.077	0.010	−0.0853
Upper transition E	0.060	−0.057	0.020	−0.082
Main				
Lower suction peak	−0.510	0.526	−0.620	0.635
Lower transition S	−0.405	0.422	−0.670	0.685
Lower transition E	−0.510	0.526	N/a	——
Upper suction peak	0.000	0.0496	0.008	0.055
Upper transition S	0.012	0.058	0.016	0.061
Upper transition E	0.025	0.068	0.025	0.068
Flap				
Lower suction peak	N/a	——	N/a	——
Lower transition S	N/a	——	N/a	——
Lower transition E	N/a	——	N/a	——
Upper suction peak (mid)	0.026	0.888	0.024	0.886
Upper suction peak (aux.)	0.020	0.882	0.016	0.878
Upper transition S	0.030	0.892	0.030	0.892
Upper transition E	0.070	0.931	0.060	0.921

equations with an upwind finite volume formulation. The code neglects viscous cross-derivative terms, which results in thin-layer Navier–Stokes equations in specified coordinate directions. For all the results in this paper, the thin-layer assumption is employed with viscous derivatives included in the direction normal to the walls only; computations with viscous terms included in both coordinate directions showed essentially no differences. The code uses third-order upwind-biased spatial differencing on the convective and pressure terms and second-order differencing on the viscous terms; it is globally second-order spatially accurate. The CFL3D code can solve flows over multiple-zone grids that are connected in a one-to-one, patched, or overset manner and can employ grid sequencing, multigrid, and local time stepping when accelerating convergence to steady state. Upwind-biased spatial differencing is used for the inviscid terms, and flux limiting is used to obtain smooth solutions in the vicinity of shock waves, when present. Viscous terms are centrally differenced. The flux-difference-splitting (FDS) method of Roe[55] is employed to obtain fluxes at the cell faces.

The CFL3D code is advanced in time with an implicit three-factor approximate factorization method. The implicit derivatives are written as spatially first-order accurate, which results in block-tridiagonal inversions for each sweep. However, for solutions that utilize FDS the block-tridiagonal inversions are further simplified with a diagonal algorithm (with a spectral radius scaling[56] of the viscous terms). Further details of the CFL3D computer code can be found in the cited references. The CFL3D code has been used successfully to compute two-dimensional multielement airfoil flowfields.[26,43] These studies included analyses of grid density effects.

When free-air grids are used, a far-field point vortex correction[57] is applied at the outer boundary. This correction has a significant impact, particularly on the computed drag for multielement airfoil flows.[13] When internal flow on a grid with walls is computed, the inflow total pressure and total temperature are specified according to isentropic flow relations, and the outflow back pressure is set to obtain the desired inflow Mach number.

V. Turbulence Modeling

The S–A[37] one-equation and SST[42] k–ω two-equation eddy-viscosity turbulence models that are employed in this study are documented in their respective references. However, the SST model has been modified slightly from its original form. Details are given in Ref. 58. [Note that an error exists in Eq. (17) in that reference. The equation should be

$$\Gamma = \max(2\Gamma_3;\ \Gamma_1) \tag{1}$$

Also, in Eq. (1) in that reference the terms $\sigma^* \mu_t$ and $\sigma \mu_t$ should be replaced with $\mu + \sigma^* \mu_t$ and $\mu + \sigma \mu_t$, respectively.]

The explicit algebraic stress model (EASM) of Gatski and Speziale[46] represents an effective compromise between the full second-moment closure and a two-equation eddy-viscosity model. This model extracts an algebraic relationship between the turbulent Reynolds stress and the mean velocity field by assuming equilibrium hypotheses on the convective terms of the Reynolds stress transport equation, neglecting diffusive effects, and assuming a tensorially linear pressure strain correlation. The EASM model requires a two-equation platform; it was first implemented in CFL3D by Abid et al.[59] in both the k–ω and k–ε formulations. Further modifications to the model have been made since that time.[60] For the results in this paper, the model is implemented in the k–ω formulation as follows:

$$\frac{Dk}{Dt} = P_k - \omega k + \frac{1}{\rho}\frac{\partial}{\partial x_j}\left[\left(\mu + \frac{\mu_t^*}{\sigma_k}\right)\frac{\partial k}{\partial x_j}\right] \tag{2}$$

$$\frac{D\omega}{Dt} = P_\omega - \beta\omega^2 + \frac{1}{\rho}\frac{\partial}{\partial x_j}\left[\left(\mu + \frac{\mu_t^*}{\sigma_\omega}\right)\frac{\partial \omega}{\partial x_j}\right] \tag{3}$$

where the production terms are

$$P_k = -\tau_{ij}\frac{\partial u_i}{\partial x_j} \tag{4}$$

and

$$P_\omega = \Upsilon\frac{\omega}{k}\left(-\tau_{ij}\frac{\partial u_i}{\partial x_j}\right) \tag{5}$$

and $\sigma_k = 1.4$, $\sigma_\omega = 2.2$, $\beta = 0.83$, $\Upsilon = \beta - [\kappa^2/\sigma_\omega\sqrt{c_\mu^*}]$, and $\kappa = 0.41$. The equilibrium eddy-viscosity term employed in the diffusion terms of Eqs. (2) and (3) is given by

$$\mu_t^* = c_\mu^*(\rho k/\omega) \tag{6}$$

where $c_\mu^* = 0.081$.

The explicit nonlinear constitutive equation that is used to close the Reynolds-averaged Navier–Stokes equations is given (after regularization) by

$$\rho\tau_{ij} = \frac{2}{3}\rho k\delta_{ij} - 2\mu_t\left(S_{ij} - \frac{1}{3}S_{kk}\delta_{ij}\right) - \frac{2\mu_t'\alpha_3}{\omega}(S_{ik}W_{kj} + S_{jk}W_{ki})$$
$$+ \frac{4\mu_t'\alpha_2}{\omega}\left(S_{ik}S_{kj} - \frac{1}{3}S_{kl}S_{kl}\delta_{ij}\right) \tag{7}$$

where

$$S_{ij} = \frac{1}{2}\left(\frac{\partial u_i}{\partial x_j} + \frac{\partial u_j}{\partial x_i}\right) \tag{8}$$

and

$$W_{ij} = \frac{1}{2}\left(\frac{\partial u_i}{\partial x_j} - \frac{\partial u_j}{\partial x_i}\right) \tag{9}$$

are the mean-rate-of-strain tensor and the mean-vorticity tensor, respectively. The turbulent viscosity μ_t is

$$\mu_t = c_\mu(\rho k/\omega) \tag{10}$$

and

$$c_\mu = \frac{3(1+\eta^2) + 0.2(\eta^6 + \zeta^6)}{3 + \eta^2 + 6\zeta^2\eta^2 + 6\zeta^2 + \eta^6 + \zeta^6}\alpha_1 \tag{11}$$

$$\eta = (\alpha_2/\omega)(S_{ij}S_{ij})^{\frac{1}{2}} \tag{12}$$

$$\zeta = (\alpha_3/\omega)(W_{ij}W_{ij})^{\frac{1}{2}} \tag{13}$$

where $\alpha_1 = (4/3 - C_2)(g/2)$, $\alpha_2 = (2 - C_3)(g/2)$, $\alpha_3 = (2 - C_4)(g/2)$, and $g = (C_1/2 + C_5 - 1)^{-1}$. The constants that govern the pressure-strain correlation model of Speziale et al.[61] are $C_1 = 6.8$, $C_2 = 0.36$, $C_3 = 1.25$, $C_4 = 0.4$, and $C_5 = 1.88$.

The μ_t' terms in Eq. (7) are given by

$$\mu_t' = c_\mu'(\rho k/\omega) \tag{14}$$

where

$$c_\mu' = \frac{3(1+\eta^2)}{3+\eta^2+6\zeta^2\eta^2+6\zeta^2+\eta^6+\zeta^6}\alpha_1 \tag{15}$$

The freestream value of k (nondimensionalized by a_∞^2) is taken to be 9×10^{-9}, and the freestream value of ω (nondimensionalized by $\rho_\infty a_\infty^2/\mu_\infty$) is taken to be 9×10^{-8}. As discussed in Ref. 62, two-equation models in the k–ω formulation can suffer from dependency on the freestream value of ω. However, computations for this study are insensitive to a large range of tested freestream values of ω from 9×10^{-4} to 9×10^{-10}.

The turbulence model equations are solved uncoupled from the Navier–Stokes equations. For the eddy-viscosity models, the only effect from turbulence is felt through the eddy viscosity term μ_t. For the EASM, additional nonlinear terms are also included in the Navier–Stokes equations. These nonlinear terms are treated explicitly, i.e., the diagonal left-hand side terms are treated with the same approximate spectral radius scaling[56] as for eddy-viscosity models.

VI. Results and Discussion

Results are computed for both the AGARD and MD configurations. Three turbulence models, the S–A and SST models and the EASM, are used for the AGARD configuration, but only the S–A model and the EASM are used for the MD configuration.

A. AGARD Configuration

For the AGARD configuration, computations are performed with transition set at $x/c = 0.125$ on the upper and lower surface of the main element and with the slat and flap computed fully turbulent. The implications of these transition settings will be discussed in the context of the MD configuration in Sec. VI.B.1.

Experimental boundary-layer profiles of the total pressure coefficient have been measured[12] at $x/c = 0.35$ on the upper surface of the main element as well as at three stations on the upper surface of the flap, as shown in Fig. 2. Results are shown for the 4.01-deg case in Figs. 3a and 3b for two of these stations. The parameter d in the figures represents the normal distance from the airfoil surface. All three models yield similar results and agree well with the experimental results, except that the EASM predicts more mixing between the flap boundary layer and main-element wake than is predicted by the other models. Also, the computations with all three turbulence models show evidence of a slat wake; the experimental results do not show this same evidence.

Although not shown here, comparisons of the computed and experimentally measured surface pressure coefficients, as well as boundary-layer profile comparisons at a higher angle of attack of 20.18 deg, can be found in Ref. 47. Overall, results for this configuration indicate that, although minor variations are evident between the three turbulence models, these models generally produce very similar surface pressure and boundary-layer total pressure predictions. Lift and drag coefficients over the range of angles of attack up to maximum lift are also predicted similarly by the three turbulence models for this case, as shown in Figs. 4a and 4b. The CFD integrated quantities compare well with the experimental results over a large range of angles of attack, but the computations overpredict

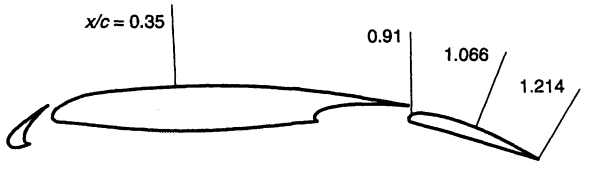

Fig. 2 AGARD profile locations.

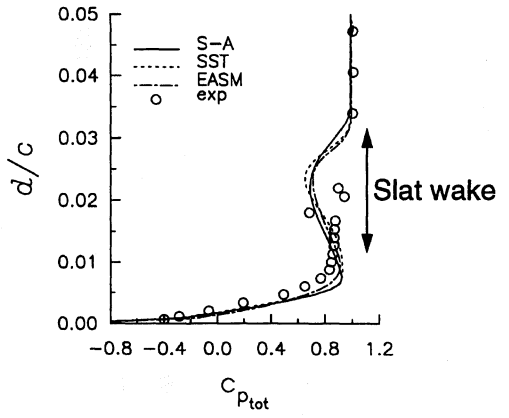

a) x/c = 0.35 (main element)

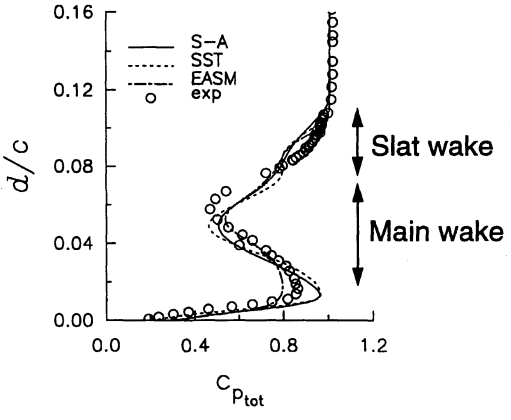

b) x/c = 1.214 (flap)

Fig. 3 AGARD total pressure coefficient profiles with α = 4.01 deg.

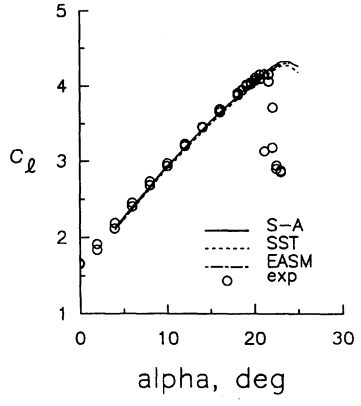

a) Lift coefficient

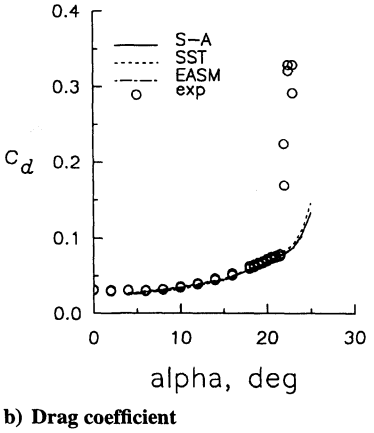

b) Drag coefficient

Fig. 4 AGARD integrated force coefficients.

the maximum lift coefficient and the angle at which maximum lift occurs. The computations also do not show the rapid dropoff of lift that occurs beyond $C_{L\,max}$, which is typical of takeoff configurations with leading-edge stall.[2]

B. MD Configuration

Most of the following results use the MD 30P-30N landing configuration at an angle of attack of 19 deg, although some results are also given for a lower angle of attack of 8 deg. Note that the hot-film data and the pressure, velocity, and skin-friction data were taken in independent wind-tunnel tests.[16–18,49] Velocity profiles are given at the locations shown in Fig. 5. When transition locations are set according to the experimental data given in Table 1, these locations are taken at the end of transition as determined from the hot-film data. One exception to this procedure is on the slat upper surface at an angle of attack of 19 deg. In this case, placing the CFD transition at the ending location results in separation because the laminar boundary layer cannot negotiate the severe adverse pressure gradient. (Although not shown, this result has also been confirmed by using a finer, embedded grid around the slat nose and with an independent boundary-layer code. Furthermore, the result is the same whether or not tunnel walls are modeled in the CFD.) Slat transition is instead placed as far downstream as possible so that the laminar boundary layer on the slat does not separate.

1. *Effect of Transition Location*

The effect of transition location is explored with the S–A turbulence model on the free-air grid only. The CFL3D code does not employ transition modeling; the code merely zeros out the production terms in the turbulence model equations in the regions in which laminar flow is desired. No transition state exists; the turbulence production is either off or on. (Turbulence transport and diffusion are always active, however.) This transition procedure is different from the trip source term procedure employed by Spalart and Allmaras.[37] The current method is used to maintain consistency between the different turbulence models in CFL3D. Fully turbulent solutions are accomplished with the production terms of the turbulence models active everywhere. Although this setting does not guarantee that a turbulent boundary layer will exist as far forward as the stagnation point, for the current applications the transition locations for fully turbulent solutions are all very close to the stagnation point of each element,[47] well forward of the experimental regions from Table 1.

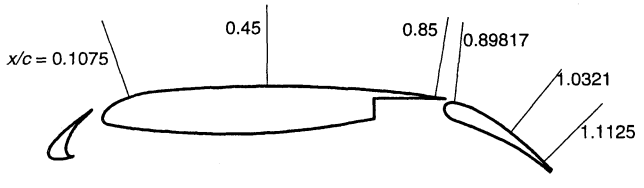

Fig. 5 30P-30N profile locations.

Figures 6a–6c show surface pressure coefficients on each element both for the fully turbulent solution and for a solution in which the transition on each element is specified according to the experimental data in Table 1. Both sets of computed results agree well with the experimental results,[16,18] with only small variations evident on the upper surfaces between the fully turbulent results and the results for which transition is specified. The transition location has only a small effect on the surface pressure for this case because the flow is well behaved (no upper-surface separation) and, as pointed out in Sec. I.A, the multielement interactions largely manipulate the inviscid flow. However, these small variations in pressure translate into a difference in lift coefficient of approximately 0.12, which is 2.7% of the lift value and is of the same order of magnitude as the experimental differences in lift coefficient that are attributable to small flap rigging changes.[1] Furthermore, as will be shown next, the velocity field is quite sensitive to transition location. Because viscous effects are a contributing factor to skin-friction forces, possible boundary-layer separation, and the stall process governed by the unloading of the aft end of the main element, the accurate prediction of boundary-layer and wake profiles is necessary. Therefore, the effects of transition location are important and need to be examined carefully.

The effect of the main-element transition location is demonstrated in Figs. 7a and 7b. The velocity profiles at two stations are shown for the case of a fully turbulent main element and for the case of transition on the main-element upper surface set close to the end-of-transition location given in Table 1. The slat and flap are both fully turbulent in these cases. When the main element is fully turbulent, its boundary-layer profile (below the slat wake in Fig. 7a) is too thick in comparison with the experimental results.[16] When transition is set, the agreement between the computed and the experimental results for the profile below the slat wake improves. The portion of the wake that results from the main-element upper surface boundary layer, i.e., the upper part of the main wake in Fig. 7b is also predicted better when the main element transition is specified. Although not shown, the computed skin-friction coefficient on the main element also agrees better with the experimental results when transition is set.[47]

Figures 7a and 7b show that when the slat is fully turbulent the slat wake is predicted to be too wide and too deep. Because the slat transition location is likely to have a large influence on the slat–wake structure over the downstream elements, we next turn our attention to an investigation of its effects. Both the upper and lower surfaces of the slat contribute to the shape of the slat wake. However, because the flow over the lower surface is further complicated by separation and then reattachment in the cove, we focus our attention solely on the effect of the slat upper surface transition location. Transition on the lower surface is set at the cusp for all cases shown here.

Unfortunately, the upper surface transition location on the slat cannot be pushed farther downstream than approximately $x/c = -0.0847$ while maintaining an attached laminar boundary layer

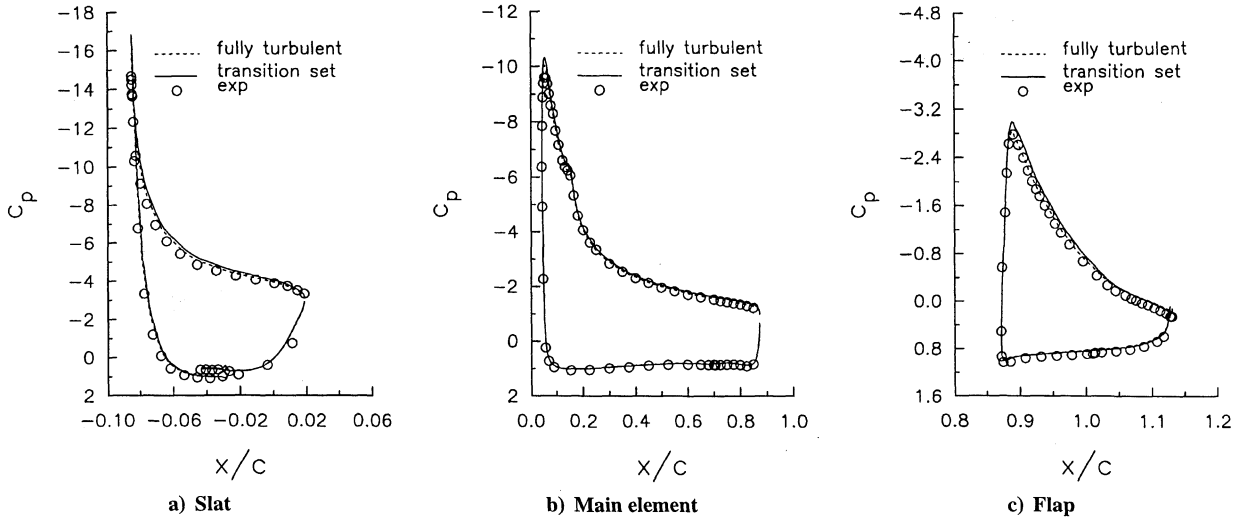

Fig. 6 Effect of transition location on 30P-30N surface pressure coefficient for S–A model on free-air grid with α = 19 deg.

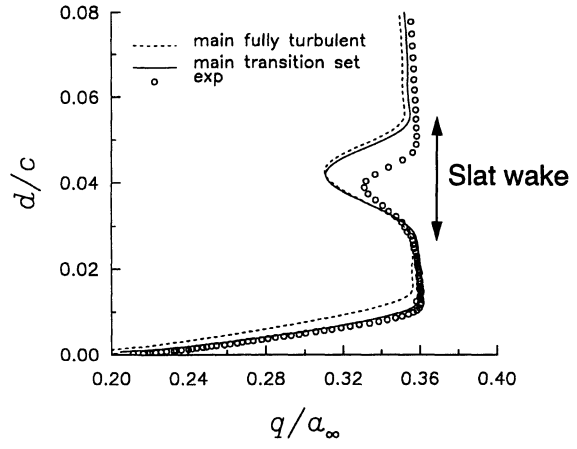

a) x/c = 0.45 (main element)

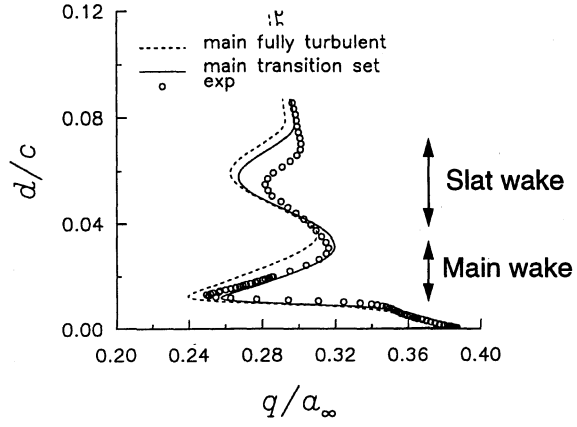

b) x/c = 0.89817 (flap)

Fig. 7 Effect of main-element transition location on 30P-30N velocity profiles for S–A model on free-air grid with α = 19 deg.

(the experimental transition range from Table 1 is $x/c = -0.0853$ to $x/c = -0.082$). To effectively force transition farther downstream, we employ suction over a small region on the slat in the computations to prevent the laminar boundary layer from separating. Computed velocity profiles are shown in Figs. 8a–8c. Locations A, B, and C correspond to $x/c = -0.0847$, -0.082, and -0.073, respectively. Their locations relative to the starting and ending locations from Table 1 are shown in Fig. 9. The wake velocity profiles that result from transition at location C agree best with the experimental profiles, although differences still exist between the computations and the experimental results, particularly in the region in which the slat wake and the main boundary layer merge at $x/c = 0.85$. In the notation of Squire[33] (discussed in Sec. I.C), the latter station is located in the region of initial merging, whereas the first two stations are in the unmerged regime. Note that transition location C is downstream of the experimentally measured transition region.

Even at the first station $x/c = 0.1075$ (Fig. 8a), the wakes that are predicted using a fully turbulent slat or using slat transition locations A or B have deficits and thicknesses that are too large. (The difference in edge velocity between the computational and experimental results in this figure is probably a result of improper calibration in the experimental data.) The computed slat–wake width and deficit using location C roughly agree with those measured experimentally at this first station, as well as over the entire length of the main element. This general agreement indicates that the S–A turbulence model does a fairly good job in representing the wake development given a good initial profile. Therefore, poor prediction of the slat wake may not be attributable to any particular failure of the turbulence model in modeling the wake but rather to the fact that the computed boundary layer that leaves the slat is too thick.

At a lower angle of attack of 8 deg, the experimental results[16] indicate an extremely diffuse slat wake at and beyond $x/c = 0.45$; the computations do not show this same result. Velocity profiles are

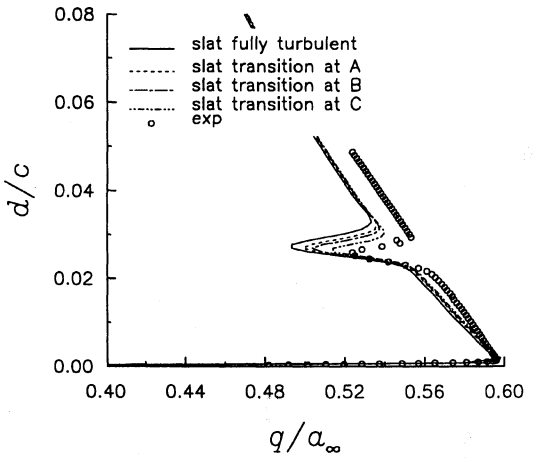

a) x/c = 0.1075 (main element)

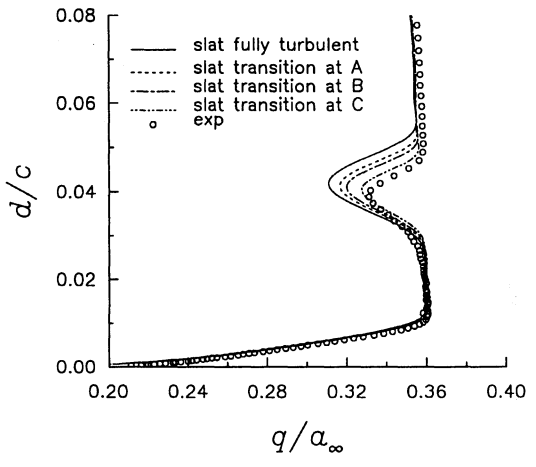

b) x/c = 0.45 (main element)

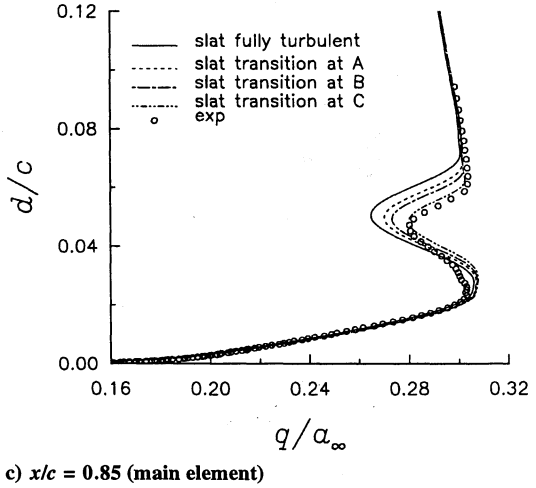

c) x/c = 0.85 (main element)

Fig. 8 Effect of slat transition location on 30P-30N velocity profiles for S–A model on free-air grid with α = 19 deg.

shown in Figs. 10a and 10b at the first two stations of the main element only. (Results at $x/c = 0.85$ are similar.) When the slat is fully turbulent, the computed slat wake is too deep and too wide at the first station $x/c = 0.1075$ and remains so farther downstream. However, even moving the slat transition location to D, i.e., $x/c = -0.056$, which is the approximate end of transition based on the experimental results, or to E, i.e., $x/c = 0.015$, near the slat trailing edge, yields a wake deficit that is still too large. (In this case, boundary-layer suction is not necessary to move the transition location downstream because the adverse pressure gradient is not too severe for the laminar boundary layer to handle.) Therefore, at this angle of attack, no upper surface slat transition location provides satisfactory slat–wake

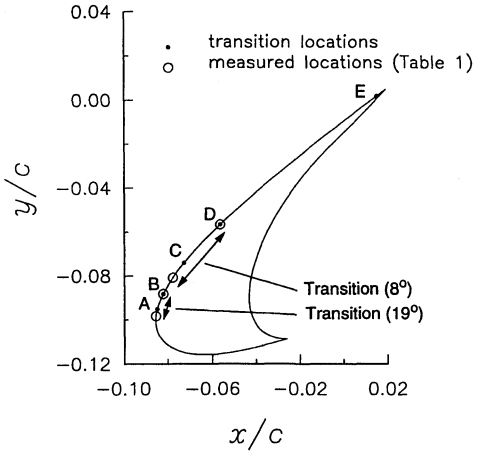

Fig. 9 30P-30N upper surface slat transition locations.

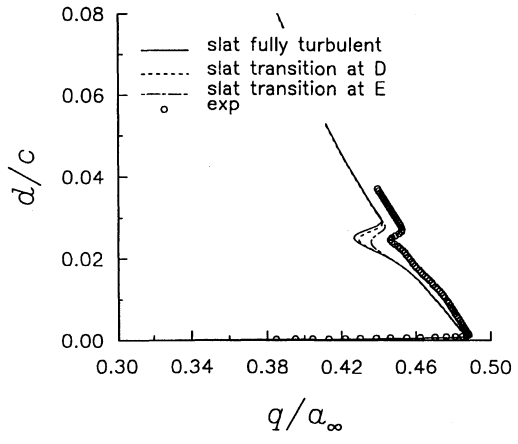

a) *x/c* = 0.1075 (main element)

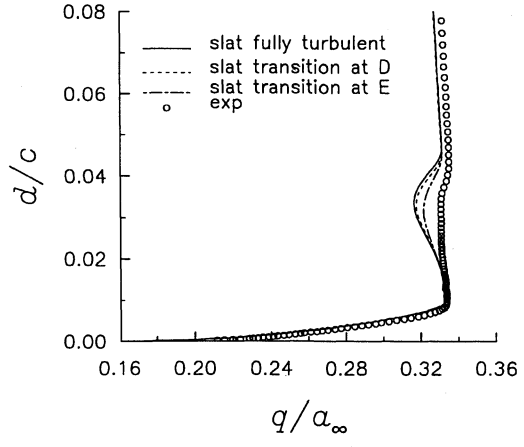

b) *x/c* = 0.45 (main element)

Fig. 10 Effect of slat transition location on 30P-30N velocity profiles for S–A model on free-air grid with α = 8 deg.

profiles that agree well with the experimental results. Although not shown, the results with the EASM are similar.

At this time, the particular physical processes on the slat that are not being modeled correctly in the computations are not known. Although we strongly suspect that the primary cause relates in some manner to transition (e.g., upper and lower surface transition locations, transition modeling, laminar bubble modeling, or possible transition in the cove free-shear layer), three-dimensional effects or unsteady effects that result from the slat–cove separated flow may also be contributing factors. Certainly, inadequate turbulence modeling in the wake may be a contributing factor as well; however, no evidence has been found at this time to indicate that inadequate

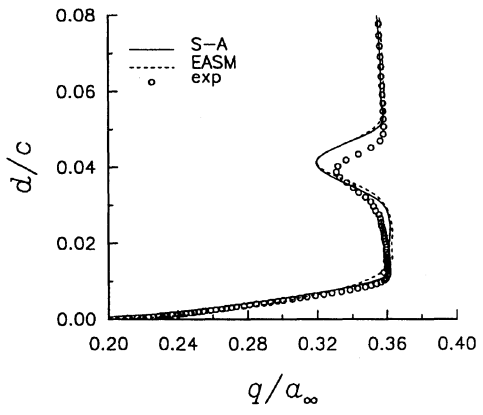

a) *x/c* = 0.45 (main element)

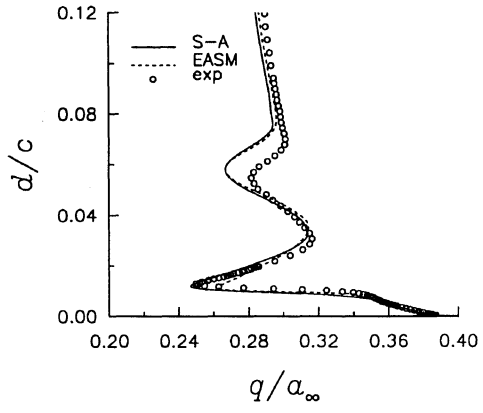

b) *x/c* = 0.89817 (flap)

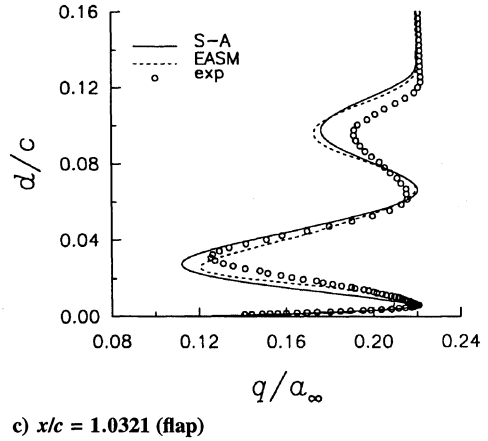

c) *x/c* = 1.0321 (flap)

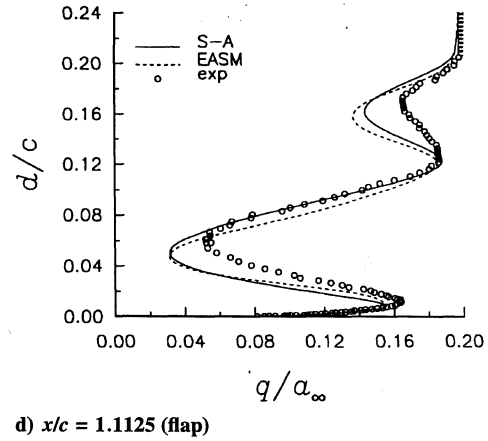

d) *x/c* = 1.1125 (flap)

Fig. 11 Effect of turbulence model on 30P-30N velocity profiles with transition set, walls modeled, and α = 19 deg.

turbulence modeling is a primary source of error. Determining the actual causes will be difficult because almost no experimental flowfield data over the slat are available at this high Reynolds number. Drawing conclusions about the ability of turbulence models to accurately predict processes such as the merging of the slat wake and the boundary layer will be difficult until we are confident that the slat flowfield and, consequently, its initial wake profile are computed adequately.

2. Effect of Turbulence Model

For the computations in this section (at 19 deg), the end-of-transition locations from the experimental results (see Table 1) are used, except that transition on the slat upper surface is placed at $x/c = -0.0847$ to avoid laminar boundary-layer separation. No boundary-layer suction is employed. As a result of the transition location studies discussed in Sec. VI.B.1, it is recognized that the flow over the slat is not modeled correctly; therefore, the results are deficient in that regard. Also, all computations in this section are performed on grids that include the tunnel walls. A description of the effects of tunnel walls can be found in Refs. 23 and 47. Velocity profiles that are computed with the S–A model and the EASM are compared in Figs. 11a–11d. The results given by the two models are quite similar. Although not shown, the turbulent shear stress profiles computed with the two turbulence models generally only exhibit minor differences.[47] An explanation for this similarity may be that this flowfield—like the AGARD flowfield—is for the most part a unidirectional shear flow (albeit a complex one). Therefore, the nonlinear constitutive relationship is probably important only in relatively small, localized regions where detailed experimental data are currently not available. Note that nonlinear terms are necessary for flows in which anisotropic turbulent stresses drive secondary flows, such as inside square ducts, or for flows with significant noninertial effects, such as in rotating channels or pipes. As mentioned in the Introduction, the extent to which nonlinear terms play a role in predicting aerodynamic flowfields of interest has yet to be determined; the current study is an initial effort to demonstrate their effect for multielement airfoil flows.

Computations with the S–A model require roughly between 3000 and 8000 multigrid cycles to converge, depending on the case and the initial conditions, at a CPU cost of approximately 10 μs per grid point per multigrid cycle on a single-processor Cray C90. The EASM is more dependent on the initial conditions and, therefore, can often require more multigrid cycles to reach convergence, at a CPU cost of approximately 13 μs per grid point per multigrid cycle.

VII. Conclusions

The flows over two different multielement airfoil configurations have been computed using linear eddy-viscosity turbulence models and a nonlinear explicit algebraic stress model. Transition locations on a McDonnell Douglas configuration that were recently measured using hot film have been presented, and the effect of transition location on the computed solutions has been explored. Based on the computed results and comparison with experimental data, the following conclusions are made.

1) Transition location is crucial to the accurate computation of boundary-layer velocity profiles. Poor boundary-layer profile predictions lead to poor trailing-edge near-wake profile predictions and, therefore, poor predictions in the far-wake region. Thus, inadequate wake predictions cannot be attributed solely to inadequate turbulence modeling but must be attributed in part to deficiencies in transition prediction on the generating element. Recently measured transition locations are helpful in this regard. Use of these locations to specify transition on the main element improves the prediction of the boundary-layer thickness, skin friction, and wake profile shape.

2) The flowfield over the slat is not well understood and is difficult to predict. Specifying transition on the slat using measured transition locations results either in slat separation or in only marginal improvement in slat–wake profiles when compared with the experimental data. Possible reasons for this disagreement include the fact that most CFD codes do not model the transition process, which may be more important on the slat than on the other elements; the possibility that the hot-film array used to measure the transition locations may have some effect on the flowfield and possibly on the transition locations; and the fact that important slat physics, e.g., possible three-dimensional effects, laminar separation bubbles, and shear-layer transition and unsteadiness in the cove region, are not modeled in the computations. Future CFD efforts in this area may be hampered by the fact that detailed experimental flowfield measurements can be difficult to obtain in the slat region, particularly at high Reynolds numbers, because of the smaller scales. However, because the computation of the slat flowfield remains a primary obstacle in the successful prediction of multielement flows, additional experimental efforts to document the flow physics in this region may be prudent.

3) Although some variations are evident, the nonlinear explicit algebraic stress turbulence model overall yields results that are similar to linear eddy-viscosity turbulence models.

Acknowledgments

The authors thank W. T. Jones of Geolab at NASA Langley Research Center for generating the MD configuration grids and J. B. Anders Jr. and C. B. McGinley of the Flow Modeling and Control Branch of NASA Langley Research Center for their help and useful discussions. The authors also acknowledge F. W. Spaid of The Boeing Company for his suggestion that the difference in edge velocity between the computational and experimental results in Fig. 8 was probably a result of improper calibration in the experimental data. Finally, the authors acknowledge S. E. Rogers of NASA Ames Research Center, P. R. Spalart of The Boeing Company, and W. K. Anderson of NASA Langley Research Center for their assistance and insightful comments.

References

[1]Lynch, F. T., Potter, R. C., and Spaid, F. W., "Requirements for Effective High Lift CFD," *International Council of the Aeronautical Sciences Proceedings, 20th Congress*, Vol. 2, AIAA, Reston, VA, 1996, pp. 1479–1492.

[2]Haines, A. B., "Scale Effects on Aircraft and Weapon Aerodynamics," AGARD-AG-323, July 1994.

[3]Yip, L. P., Vijgen, P. M. H. W., Hardin, J. D., and VanDam, C. P., "In-Flight Pressure Distributions and Skin-Friction Measurements on a Subsonic Transport High-Lift Wing Section," CP-515, AGARD, Sept. 1993, pp. 21.1–21.19.

[4]Kirkpatrick, D., and Woodward, D., "Priorities for High-Lift Testing in the 1990's," AIAA Paper 90-1413, June 1990.

[5]Ying, S. X., "High Lift: Challenges and Directions for CFD," *Proceedings of the Northwestern Polytechnical University/AIAA Atmospheric Flight Mechanics Conference*, Northwestern Polytechnical Univ., Xian, PRC, 1996, pp. 164–177.

[6]Meredith, P. T., "Viscous Phenomena Affecting High-Lift Systems and Suggestions for Future CFD Development," CP-515, AGARD, Sept. 1993, pp. 19.1–19.8.

[7]Smith, A. M. O., "High Lift Aerodynamics," *Journal of Aircraft*, Vol. 12, No. 6, 1975, pp. 501–530.

[8]Woodward, D. S., and Lean, D. E., "Where is High Lift Today?—A Review of Past UK Research Programmes," CP-515, AGARD, Sept. 1993, pp. 1.1–1.45.

[9]Thibert, J. J., Reneaux, J., Moens, F., and Preist, J., "ONERA Activities on High-Lift Devices for Transport Aircraft," *Proceedings of Royal Aeronautical Society High Lift and Separation Control*, Royal Aeronautical Society, London, 1995, pp. 5.1–5.18.

[10]Valarezo, W. O., "Topics in High-Lift Aerodynamics," AIAA Paper 93-3136, July 1993.

[11]Drela, M., "Newton Solution of Coupled Viscous/Inviscid Multielement Airfoil Flows," AIAA Paper 90-1470, June 1990.

[12]Burt, M., "A Selection of Experimental Test Cases for the Validation of CFD Codes: Chapter 5—Summaries of the Test Cases," AGARD AR-303, Vol. 1, Aug. 1994, pp. 55–133.

[13]Fejtek, I., "Summary of Code Validation Results for a Multiple Element Airfoil Test Case," AIAA Paper 97-1932, July 1997.

[14]Stainback, P. C., McGhee, R. J., Beasley, W. D., and Morgan, H. L., Jr., "The Langley Research Center's Low Turbulence Pressure Tunnel," AIAA Paper 86-0762, March 1986.

[15]Paschal, K., Goodman, W., McGhee, R., Walker, B., and Wilcox, P. A., "Evaluation of Tunnel Sidewall Boundary-Layer-Control Systems for High-Lift Airfoil Testing," AIAA Paper 91-3243, Sept. 1991.

[16]Spaid, F. W., and Lynch, F. T., "High Reynolds Number Multi-Element Airfoil Flowfield Measurements," AIAA Paper 96-0682, Jan. 1996.

[17]Klausmeyer, S. M., and Lin, J. C., "An Experimental Investigation of Skin Friction on a Multi-Element Airfoil," AIAA Paper 94-1870, June 1994.

[18]Chin, V. D., Peters, D. W., Spaid, F. W., and McGhee, R. J., "Flowfield Measurements About a Multi-Element Airfoil at High Reynolds Numbers," AIAA Paper 93-3137, July 1993.

[19]Valarezo, W. O., Dominik, C. J., and McGhee, R. J., "Reynolds and Mach Number Effects on Multielement Airfoils," *Proceedings of 5th Symposium on Numerical and Physical Aspects of Aerodynamic Flows*, California State Univ., Long Beach, CA, 1992, pp. 6.1–6.13; also NASA CR-193000, Pt. 1, Jan. 1992.

[20]Valarezo, W. O., Dominik, C. J., McGhee, R. J., Goodman, W. L., and Paschal, K. B., "Multi-Element Airfoil Optimization for Maximum Lift at High Reynolds Numbers," AIAA Paper 91-3332, Sept. 1991.

[21]Rogers, S. E., "Progress in High-Lift Aerodynamic Calculations," AIAA Paper 93-0194, Jan. 1993.

[22]Dominik, C. J., "Application of the Incompressible Navier–Stokes Equations to High-Lift Flows," AIAA Paper 94-1872, June 1994.

[23]Cao, H. V., Kusunose, K., Spalart, P. R., Ishimitsu, K. K., Rogers, S. E., and McGhee, R. J., "Study of Wind Tunnel Wall Interference for Multi-Element Airfoils Using a Navier–Stokes Code," AIAA Paper 94-1933, June 1994.

[24]Rogers, S. E., Menter, F. R., Durbin, P. A., and Mansour, N. N., "A Comparison of Turbulence Models in Computing Multi-Element Airfoil Flows," AIAA Paper 94-0291, Jan. 1994.

[25]Kusunose, K., and Cao, H. V., "Prediction of Transition Location for a 2-D Navier–Stokes Solver for Multi-Element Airfoil Configurations," AIAA Paper 94-2376, June 1994.

[26]Jones, K. M., Biedron, R. T., and Whitlock, M., "Application of a Navier–Stokes Solver to the Analysis of Multielement Airfoils and Wings Using Multizonal Grid Techniques," AIAA Paper 95-1855, June 1995.

[27]Valarezo, W. O., and Mavriplis, D. J., "Navier–Stokes Applications to High-Lift Airfoil Analysis," AIAA Paper 93-3534, Aug. 1993.

[28]Anderson, W. K., Bonhaus, D. L., McGhee, R. J., and Walker, B. S., "Navier–Stokes Computations and Experimental Comparisons for Multielement Airfoil Configurations," *Journal of Aircraft*, Vol. 32, No. 6, 1995, pp. 1246–1253.

[29]Cao, H. V., and Kusunose, K., "Grid Generation and Navier–Stokes Analysis for Multi-Element Airfoils," AIAA Paper 94-0748, Jan. 1994.

[30]Kusunose, K., and Cao, H. V., "Numerical Prediction of Reverse Reynolds Number Effects for Multi-Element Airfoils," *Numerical Methods in Laminar and Turbulent Flow*, edited by C. Taylor and P. Durbetaki, Vol. 9, Pt. 1, Pineridge, Swansea, Wales, UK, 1995, pp. 457–468.

[31]Cebeci, T., "Calculation of Multielement Airfoils and Wings at High Lift," CP-515, AGARD, Sept. 1993, pp. 24.1–24.15.

[32]Arlinger, B. G., Larsson, T., Arnold, F., Earnshaw, P. B., Moens, F., Saliveros, E., and Termes, A. P. P., "Reynolds- and Mach-Number Effects and 2D-3D Correlation Based on Measurements and Computed Results for the GARTEUR Take-Off Configuration," *Proceedings of Royal Aeronautical Society High Lift and Separation Control*, Royal Aeronautical Society, London, 1995, pp. 26.1–26.15.

[33]Squire, L. C., "Interactions Between Wakes and Boundary Layers," *Progress in Aerospace Sciences*, Vol. 26, No. 3, 1989, pp. 261–288.

[34]Agoropoulos, D., and Squire, L. C., "Interactions Between Turbulent Wakes and Boundary Layers," *AIAA Journal*, Vol. 26, No. 10, 1988, pp. 1194–1200.

[35]Anderson, W. K., and Bonhaus, D. L., "Navier–Stokes Computations and Experimental Comparisons for Multielement Airfoil Configurations," AIAA Paper 93-0645, Jan. 1993.

[36]Nakayama, A., Kreplin, H. P., and Morgan, H. L., "Experimental Investigation of Flowfield About a Multielement Airfoil," *AIAA Journal*, Vol. 28, No. 1, 1990, pp. 14–21.

[37]Spalart, P., and Allmaras, S., "A One-Equation Turbulence Model for Aerodynamic Flows," *La Recherche Aerospatiale*, No. 1, 1994, pp. 5–21.

[38]Lien, F. S., and Leschziner, M. A., "Modelling 2D Separation from a High Lift Aerofoil with a Non-Linear Eddy-Viscosity Model and Second-Moment Closure," *Aeronautical Journal of the Royal Aeronautical Society*, Vol. 99, April 1995, pp. 125–144.

[39]Lien, F. S., Chen, W. L., and Leschziner, M. A., "Computational Modelling of High-Lift Aerofoils with Turbulence-Transport Models," *Proceedings of Royal Aeronautical Society High Lift and Separation Control*, Royal Aeronautical Society, London, 1995, pp. 10.1–10.14.

[40]Van den Berg, B., "Boundary Layer Measurements on a Two-Dimensional Wing with Flap," National Aerospace Lab., NLR TR 79009 U, Amsterdam, The Netherlands, Jan. 1979.

[41]Godin, P., Zingg, D. W., and Nelson, T. E., "High-Lift Aerodynamic Computations with One- and Two-Equation Turbulence Models," *AIAA Journal*, Vol. 35, No. 2, 1997, pp. 237–243.

[42]Menter, F. R., "Improved Two-Equation $k-\omega$ Turbulence Models for Aerodynamic Flows," NASA TM-103975, Oct. 1992.

[43]Jasper, D. W., Agrawal, S., and Robinson, B. A., "Navier–Stokes Calculations on Multi-Element Airfoils Using a Chimera-Based Solver," CP-515, AGARD, Sept. 1993, pp. 8.1–8.11.

[44]Fritz, W., "Calculation of Maximum and High Lift Characteristics of Multi Element Airfoils," CP-515, AGARD, Sept. 1993, pp. 5.1–5.12.

[45]Kral, L. D., Mani, M., and Ladd, J. A., "On the Application of Turbulence Models for Aerodynamic and Propulsion Flowfields," AIAA Paper 96-0564, Jan. 1996.

[46]Gatski, T. B., and Speziale, C. G., "On Explicit Algebraic Stress Models for Complex Turbulent Flows," *Journal of Fluid Mechanics*, Vol. 254, 1993, pp. 59–78.

[47]Rumsey, C. L., Gatski, T. B., Ying, S. X., and Bertelrud, A., "Prediction of High-Lift Flows Using Turbulent Closure Models," AIAA Paper 97-2260, June 1997.

[48]Nakayama, A., Stack, J. P., Lin, J. C., and Valarezo, W. O., "Surface Hot-Film Technique for Measurements of Transition, Separation, and Reattachment Points," AIAA Paper 93-2918, July 1993.

[49]Bertelrud, A., "Transition on a Three-Element High Lift Configuration at High Reynolds Numbers," AIAA Paper 98-0703, Jan. 1998.

[50]Bertelrud, A., Johnson, S., Lytle, C., and Mills, C., "A System for Analysis of Transition Characteristics on a High-Lift Configuration at High Reynolds Numbers," *17th International Congress on Instrumentation in Aerospace Simulation Facilities*, edited by F. K. Owen, Inst. of Electrical and Electronics Engineers, Piscataway, NJ, 1997, pp. 141–152.

[51]Thomas, J. L., Krist, S. L., and Anderson, W. K., "Navier–Stokes Computations of Vortical Flows Over Low Aspect-Ratio Wings," *AIAA Journal*, Vol. 28, No. 2, 1990, pp. 205–212.

[52]Vatsa, V. N., Thomas, J. L., and Wedan, B. W., "Navier–Stokes Computations of Prolate Spheroids at Angle of Attack," *Journal of Aircraft*, Vol. 26, No. 11, 1989, pp. 986–993.

[53]Thomas, J. L., "Reynolds Number Effects on Supersonic Asymmetrical Flows over a Cone," *Journal of Aircraft*, Vol. 30, No. 4, 1993, pp. 488–495.

[54]Rumsey, C. L., Sanetrik, M. D., Biedron, R. T., Melson, N. D., and Parlette, E. B., "Efficiency and Accuracy of Time-Accurate Turbulent Navier–Stokes Computations," *Computers and Fluids*, Vol. 25, No. 2, 1996, pp. 217–236.

[55]Roe, P., "Approximate Riemann Solvers, Parameter Vectors, and Difference Schemes," *Journal of Computational Physics*, Vol. 43, No. 2, 1981, pp. 357–372.

[56]Coakley, T. J., "Implicit Upwind Methods for the Compressible Navier–Stokes Equations," AIAA Paper 83-1958, July 1983.

[57]Thomas, J. L., and Salas, M. D., "Far-Field Boundary Conditions for Transonic Lifting Solutions to the Euler Equations," *AIAA Journal*, Vol. 24, No. 7, 1986, pp. 1074–1080.

[58]Menter, F. R., and Rumsey, C. L., "Assessment of Two-Equation Turbulence Models for Transonic Flows," AIAA Paper 94-2343, June 1994.

[59]Abid, R., Rumsey, C. L., and Gatski, T. B., "Prediction of Nonequilibrium Turbulent Flows with Explicit Algebraic Stress Models," *AIAA Journal*, Vol. 33, No. 11, 1995, pp. 2026–2031.

[60]Gatski, T. B., "Prediction of Airfoil Characteristics with Higher Order Turbulence Models," NASA TM-110246, April 1996.

[61]Speziale, C. G., Sarkar, S., and Gatski, T. B., "Modeling the Pressure–Strain Correlation of Turbulence: An Invariant Dynamical Systems Approach," *Journal of Fluid Mechanics*, Vol. 227, 1991, pp. 245–272.

[62]Menter, F. R., "Influence of Freestream Values on $k-\omega$ Turbulence Model Predictions," *AIAA Journal*, Vol. 30, No. 6, 1992, pp. 1657–1659.

C. G. Speziale
Associate Editor